Available online at www.sciencedirect.com
ScienceDirect
Trans. Nonferrous Met. Soc. China 33(2023) 189−200
Transactions of Nonferrous Metals Society of China
www.tnmsc.cn

Hot compressive deformation and microstructural evolution of 60NiTi alloy

Dong CHEN[1], Qian-ru YANG[1], Na-chuan YANG[1], Meng WANG[1], Qiang XU[1], Jing-yuan WU[1], Yan-bin JIANG[1,2], Zhou LI[1,3], Zhu XIAO[1,3], Hai-gen WEI[4]

1. School of Materials Science and Engineering, Central South University, Changsha 410083, China;
2. Key Laboratory of Non-ferrous Metal Materials Science and Engineering, Ministry of Education, Central South University, Changsha 410083, China;
3. State Key Laboratory of Powder Metallurgy, Central South University, Changsha 410083, China;
4. Faculty of Materials Metallurgy and Chemistry, Jiangxi University of Science and Technology, Ganzhou 341000, China

Received 11 October 2021; accepted 19 January 2022

Abstract: Hot deformation behavior and microstructure of 60NiTi alloy during hot compressive deformation were investigated using Gleeble−3500 thermal simulation test machine in the temperature range of 500−650 °C and strain rate range of 0.001−1 s^{-1}. The constitutive equation of hot compression was constructed and the hot processing maps were plotted. When the compression temperature rose or the strain rate declined, the peak stress reduced. The hot deformation activation energy was calculated as 327.89 kJ/mol, and the proper hot working parameters of compression temperature of 600−650 °C and strain rate of 0.005−0.05 s^{-1} were obtained. The recrystallization degree increased with increasing compression temperature. When the strain rate increased, both dislocation density and number of twins were improved, and the Ni_3Ti phase tended to aggregate. Ni_3Ti precipitation phase was beneficial to inducing dynamic recrystallization of the 60NiTi alloy. The dynamic recovery, dynamic recrystallization and twinning took place during hot compressive deformation of the 60NiTi alloy.

Key words: 60NiTi alloy; hot compressive deformation; microstructure; dynamic recrystallization

1 Introduction

60NiTi alloy is an intermetallic compound with 55 at.% nickel and 45 at.% titanium, and has some special performances including high strength and hardness, low attenuation, non-magnetism and excellent corrosive resistance etc, which works as an ideal bearing material in aerospace and ocean engineering [1−3]. In addition, 60NiTi alloy possesses good bio-compatibility and good dimensional stability, which has a wide application prospect in biomedical field [2,4].

In order to meet shape and size requirements of bearing devices, hot rolling and hot extrusion of NiTi alloy are required [5,6]. However, many intermetallic compounds (Ni_4Ti_3, Ni_3Ti_2, and Ni_3Ti) exist in NiTi alloy, resulting in its poor workability [7]. It is difficult to control deformation of hot working process; therefore, suitable hot deformation process parameters should be given. Hot deformation of metallic material is carried out by using the thermal simulation test. Using high temperature plastic flow constitutive model and hot processing map, the rheological behavior of the material can be well understood, and the feasible processing parameters can be also determined, which has been widely used in various alloys such

Corresponding author: Yan-bin JIANG, Tel: +86-13466312126, E-mail: jiangyanbin@tsinghua.org.cn
DOI: 10.1016/S1003-6326(22)66099-0

as copper alloy [8,9], magnesium alloy [10,11] and Ni−Ti alloy [12−14]. MORAKABATI et al [14] discussed the hot compressive deformation of $Ni_{49.8}Ti_{50.2}$ alloy, and the ductility of the hot deformed alloy was the lowest in the instability region and some dynamic recrystallized grains were observed in stability region during hot deformation. YEOM et al [12] optimized the hot-forged process of as-cast Ni−44.5wt.%Ti shape memory alloy by finite element analysis and hot processing map. No defect was found in the hot-forged alloy at 1050 °C. ZHANG et al [15] reported the hot compressive deformation behavior of equiatomic NiTi alloy and obtained feasible hot working processing windows. Adiabatic shear bands were observed in the unstable domain at low temperature. Abnormal grain growth was found in the unstable region at high temperature. Compared with the above equiatomic NiTi alloys, the Ni content in 60NiTi alloy is higher and the number of intermetallic compounds (Ni_4Ti_3, Ni_3Ti_2 and Ni_3Ti) in the alloy increases obviously. Therefore, the microstructure and hot deformation behavior of 60NiTi alloy was different in the process of hot working due to the different ratio between *B*2 matrix and Ni−Ti precipitation.

In this work, the hot compressive deformation of 60NiTi alloy was investigated at temperature between 500 and 650 °C and strain rate of 0.001−1 s^{-1}. The constitutive equation of 60NiTi was built, and the hardening rate (θ) versus true stress (σ) curve and hot processing map were drawn. Its structure evolution and deformation mechanism during hot compression were discussed, which can offer a reference for hot working technology of the 60NiTi alloy.

2 Experimental

60NiTi alloy billet with diameter of 100 mm was melted in vacuum kiln and then extruded into *d*40 mm rod by hot extrusion with an extrusion ratio of 6.25 at temperature of 900 °C. The extruded rod was annealed at 650 °C for 12 h. The cylindrical hot compression specimens with 8 mm in diameter and 12 mm in height were cut by wire electrical discharge machining.

In this work, a large number of Ni_3Ti precipitates were formed in the sample after annealing at 650 °C for 12 h, which induced softening of the alloys [16], and our previous work indicated that the annealed sample can be hot worked at a deformation temperature below 650 °C. Hot compressive deformation of the samples was performed by using Gleeble−3500 thermal simulation test machine at various temperatures (500, 550, 600 and 650 °C) with diverse strain rates (0.001, 0.01, 0.1 and 1 s^{-1}), and the true strain was 0.5. The heat rate of hot compression samples was approximately 20 °C/s and the holding time was 3 min. The graphite plate was placed between the compressive samples and the penetrator. Figure 1 shows the schematic drawing of hot compression test.

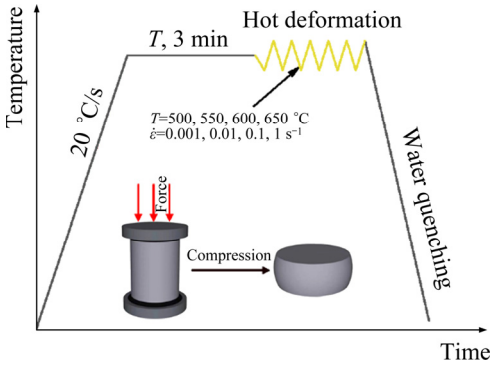

Fig. 1 Schematic diagram of hot compression test

The microstructure of the 60NiTi alloy after compressive deformation was observed by ZEISS EVO−MA10 scanning electron microscope (SEM), equipped with the energy disperse spectroscopy (EDS) to analyze chemical composition of the phases. The phases of 60NiTi alloy were also identified using X-ray diffractometry (D/max 2550). The wafers of the samples of 50 μm in thickness and 3 mm in diameter were firstly thinned using the mechanical thinning instrument, and then thinned by the Struers Tenupol−5 twin-jet electropolishing instrument with an electrolyte of 5 vol.% perchlorate acid and 95 vol.% methanol. The twin-jet electropolishing parameters were the voltage of 12 V, current of 28 mA and electrolyte temperature of approximately −35 °C. Transmission electron microscopy (TEM) observation of microstructure in the compressed samples were conducted by using Tecnai G2 F20 S−TWIN.

3 Results and discussion

3.1 True stress versus true strain curves

Figure 2 shows the true stress versus true strain

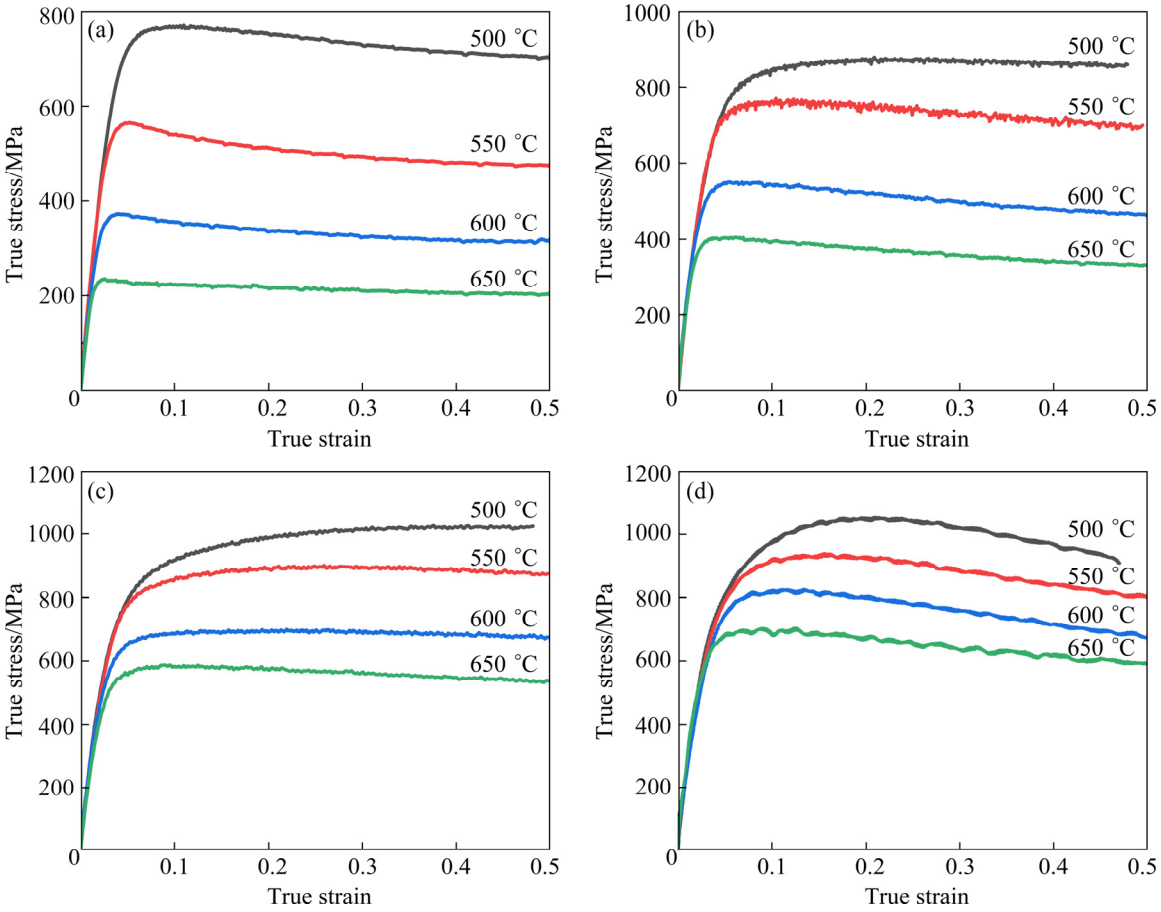

Fig. 2 True stress−true strain curves of 60NiTi alloy at different deformation temperatures and strain rates: (a) 0.001 s^{-1}; (b) 0.01 s^{-1}; (c) 0.1 s^{-1}; (d) 1 s^{-1}

curves of the 60NiTi alloy during hot compression at the temperature of 500−650 °C and the strain rate of 0.001−1 s^{-1}. From Fig. 2, the true stress of the alloy increased rapidly in the early period of deformation, then increased gradually, and finally approached to the stable stage or dropped slightly with raising the true strain. When the strain was low, the main factor for the sharp ascent of flow stress was the rapid increase of dislocation density resulting in large work-hardening effect. While the strain increased, the dislocation density increased. Meanwhile, the dynamic recrystallization (DRX) took place under the combined action of heat and stress, which resulted in slow growth of the flow stress. When the stress approached to the peak, the softening from dynamic recovery (DRV) or DRX balanced with the working hardening, and the curves came to the steady stage. In addition, the true stress versus true strain curve presented distinct zigzag characteristics at strain rate of 1 s^{-1}, as indicated in Fig. 2(d). The fluctuation of the curve was mainly attributed to the two main factors: one was the combined action of hardening effect and softening effect, and the other was the formation of twins during hot deformation [9,17]. 60NiTi alloy pertains low stacking fault energy metal, and a large number of Ni_3Ti phase precipitated in the alloy. Especially, twins preferred to form in the stress concentration region during deformation. The Ni_3Ti phase pinned dislocations, causing the substantial piling-up of dislocation around Ni_3Ti phase during hot deformation. As the deformation proceeded, the dislocation slip was impeded, and twins are easy to germinate at the stress concentration region [18]. After the formation of the twins, the stress was released quickly, which induced the sudden decline of the curves. When the hot compression proceeded, the stress kept increasing, and new stress concentration and twin occurred around Ni_3Ti phase, which caused the serrated curves.

Figure 3 shows the peak stress value with different compression parameters. While the compression temperature dropped or the strain rate grew, the peak stress rose. When the compression

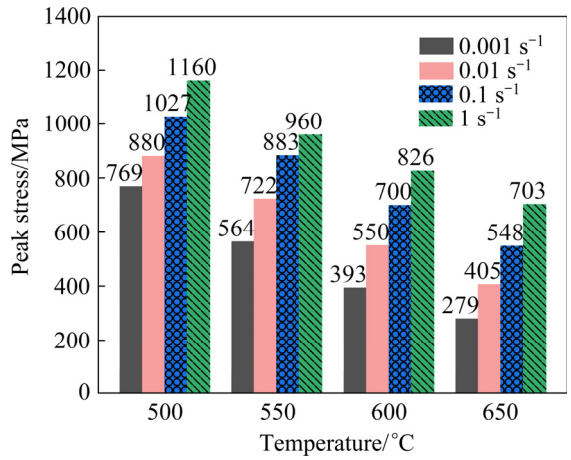

Fig. 3 Peak stresses of 60NiTi alloy under different deformation conditions

temperature was 650 °C, the peak stress declined from 703 to 279 MPa as the strain rate decreased from 1 to 0.001 s^{-1}. The peak stress decreased from 1160 MPa of 500 °C to 703 MPa of 650 °C when the strain rate was 1 s^{-1}. The diffusion ability of alloy atoms was high at high compression temperature, which resulted in high nucleation ratio and growth rate of dynamic recrystallization grains. Therefore, the more dislocations were consumed, which resulted in the increase of the softening effect and the reduction of the peak stress. Additionally, when the strain rate was lower, time for DRX nucleation and growth was longer, which caused the greater softening effect and the smaller peak stress [19].

According to the above analysis, dislocation density gradually increased with the strain. When dislocation density increased to a critical value, DRX took place, which affected the hardening behavior and deformation mechanism [20]. By fitting and differentiating the true stress−true strain curves, the variation of the work hardening rate θ with true stress σ can be obtained. The inflection point of θ–σ curves represented the critical value of the DRX occurrence [21]. Figure 4(a) shows θ–σ curves at strain rate of 0.1 s^{-1}, and the circle in the figure represented the critical value of occurrence of the DRX. Additionally, θ equaled 0 at the peak stress. From Fig. 4(a), the θ–σ curves showed similar characteristics at various compression temperatures. The slope of the curve was sharp in the early period of deformation. Moreover, with the increment of stress, the softening effect caused by DRV was less than the

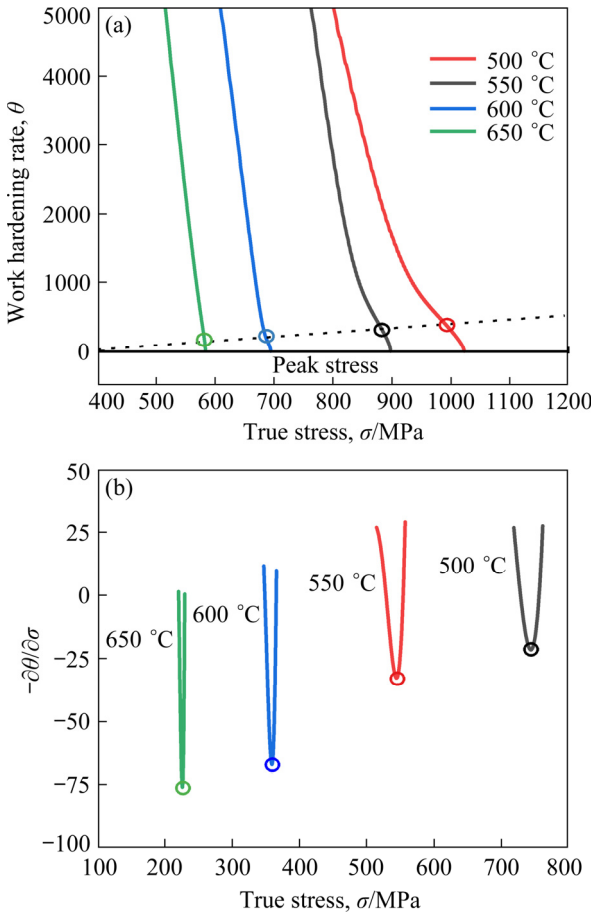

Fig. 4 Relationship between θ and σ at different strain rates: (a) 0.1 s^{-1}; (b) 0.001 s^{-1}

work hardening effect induced by the high dislocation density, which reduced the value of θ [22]. With further increase of dislocation density, when the dislocation density approached to the critical value (corresponding to the inflection point on the curve of Fig. 4(a)), DRX occurred, and the rapid decline of work hardening rate made the stress slowly approach to the peak stress (corresponding to θ=0). POLIAK and JONAS [23] determined the inflection point of the θ–σ curves by the extreme points of $(\partial\theta/\partial\sigma)$–$\sigma$ curves. Figure 4(b) showed that on the $(\partial\theta/\partial\sigma)$–$\sigma$ curves at strain rate of 0.001 s^{-1}, the critical stress dropped with the increase of compression temperature.

3.2 Flow stress constitutive equation

Based on the true stress−true strain curves of 60NiTi alloy in Fig. 1, the peak stress was closely associated with the compression temperature and the strain rate. Arrhenius equation can describe the relationship, as given in Eq. (1) [24]:

$$\dot{\varepsilon}=A\cdot[\sinh(\alpha\sigma)]^n\exp\left(-\frac{Q}{RT}\right) \quad (1)$$

where Q is the activation energy (kJ/mol), $\dot{\varepsilon}$ is strain rate (s^{-1}), σ is peak stress or flow stress (MPa), T is compression temperature (K), R is molar gas constant (8.314 J/(mol·K)), and α, A and n are material constants.

According to the stress magnitude, Eq. (1) can be rewritten as follows:

$$\dot{\varepsilon}=A_1\sigma^n\exp[-Q/(RT)],\ \alpha\sigma<0.8 \quad (2)$$

$$\dot{\varepsilon}=A_2\exp(\beta\sigma)\exp[-Q/(RT)],\ \alpha\sigma>1.2 \quad (3)$$

$$\beta=n\alpha \quad (4)$$

Zener−Hollomon parameter, Z, can describe the relationship between strain rate and compression temperature [25]:

$$Z=\dot{\varepsilon}\exp[Q/(RT)]=A\sigma[\sinh(\alpha\sigma)]^n \quad (5)$$

Equations (1)−(3) can be rewritten in the logarithm form as follows:

$$\ln\dot{\varepsilon}=\ln A-Q/(RT)+n\ln[\sinh(\alpha\sigma)] \quad (6)$$

$$\ln\dot{\varepsilon}=\ln A_1+n\ln\sigma-Q/(RT) \quad (7)$$

$$\ln\dot{\varepsilon}=\ln A_2+\beta\sigma-Q/(RT) \quad (8)$$

From Eqs. (7) and (8), when the compression temperature is a constant, the curves of $\ln\dot{\varepsilon}-\ln\sigma$ and $\sigma-\ln\dot{\varepsilon}$ were in the liner relationship, and $1/n$ and $1/\beta$ are the slopes of the $\ln\sigma-\ln\dot{\varepsilon}$ curve and the $\sigma-\ln\dot{\varepsilon}$ curve, respectively. The $\sigma-\ln\dot{\varepsilon}$ curve was indicated in Fig. 5(a) and the average slope value of $\sigma-\ln\dot{\varepsilon}$ curve was calculated as $\beta=2.1\times10^{-2}$ MPa^{-1}. From Fig. 5(b), the average slope value can be calculated as $n=7.8$. Therefore, α can be calculated from Eq. (4), namely $\alpha=\beta/n=2.7\times10^{-3}$ MPa^{-1}.

When compression temperature is a constant, Eq. (6) is rewritten as follows:

$$n=[\partial\ln\dot{\varepsilon}/\partial\ln[\sinh(\alpha\sigma)]]_T \quad (9)$$

If the strain rate is a constant, Eq. (6) is rewritten as follows:

$$Q/(Rn)=\left[\partial\ln[\sinh(\alpha\sigma)]/\partial(1/T)\right]_{\dot{\varepsilon}} \quad (10)$$

From Eqs. (9) and (10), the hot deformation activation energy Q is written by

$$Q=R\left[\partial\ln[\sinh(\alpha\sigma)]/\partial(1/T)\right]_{\dot{\varepsilon}}\cdot\left[\partial\ln\dot{\varepsilon}/\partial\ln[\sinh(\alpha\sigma)]\right]_T \quad (11)$$

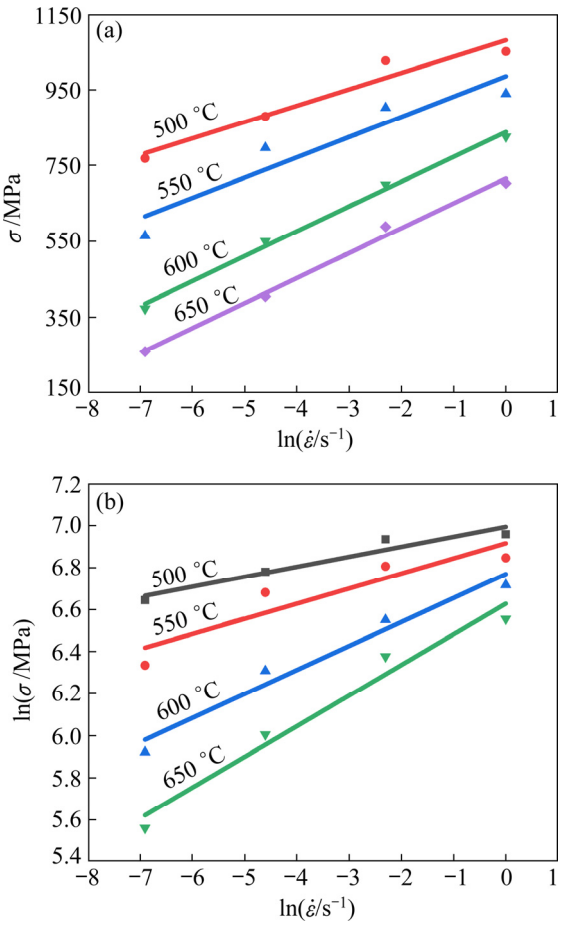

Fig. 5 Relationship between peak stress and strain rate: (a) $\sigma-\ln\dot{\varepsilon}$ curve; (b) $\ln\sigma-\ln\dot{\varepsilon}$ curve

Figures 6(a, b) showed the $\ln[\sinh(\alpha\sigma)]-\ln\dot{\varepsilon}$ curve and $\ln[\sinh(\alpha\sigma)]-1/T$ curve, respectively. From Eq. (11), the deformation activation energy Q was 327.89 kJ/mol. Equation (5) can be written by

$$\ln Z=\ln A+n\ln[\sinh(\alpha\sigma)] \quad (12)$$

Figure 7 shows the linear relationship between $\ln Z$ and $\ln[\sinh(\alpha\sigma)]$. The value of A can be calculated to be 9.0×10^{15} by fitting the relationship of $\ln Z$ and $\ln[\sinh(\alpha\sigma)]$. Replacing Q, A, α, and n into Eq. (1), the constitutive equation of the 60NiTi can be determined as

$$\dot{\varepsilon}=9.0\times10^{15}[\sinh(2.7\times10^{-3}\sigma)]^{5.7}\cdot\exp[-327887.5/(RT)] \quad (13)$$

$$Z=\dot{\varepsilon}\exp[327887.5/(RT)] \quad (14)$$

To assess the precision of the flow stress constitutive equation, the peak stresses under various compression conditions were calculated and contrasted with the experimental values according to Eq. (13), as shown in Fig. 6. By Eq. (15), the relative error (r) between the measured stress value

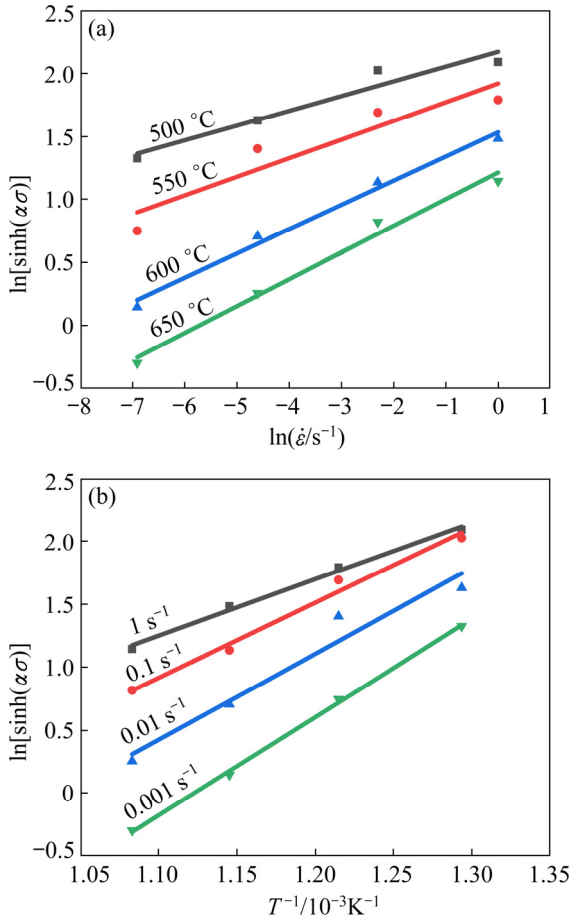

Fig. 6 Linear relationship of $\ln[\sinh(\alpha\sigma)]-\ln\dot{\varepsilon}$ (a) and $\ln[\sinh(\alpha\sigma)]-1/T$ (b)

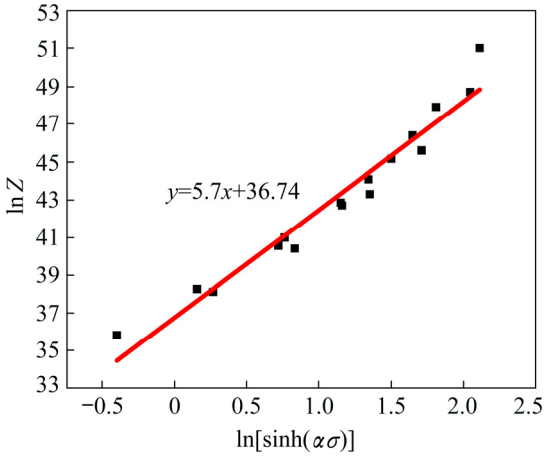

Fig. 7 Linear relationship between ln Z and $\ln[\sinh(\alpha\sigma)]$

and calculated one can be calculated, and the results are shown in Fig. 8.

$$r=\frac{\sigma_c-\sigma_m}{\sigma_m}\times 100\% \tag{15}$$

where σ_c is the calculated value of the peak stress, and σ_m is the measured value of peak stress. In accordance with the results in Fig. 8, the maximum error was −4.5%, the minimum error was −1.1% and the average error was 2.9%, which indicated that the calculated Arrhenius constitutive equation had high accuracy and can better predict peak stress of the 60NiTi alloy.

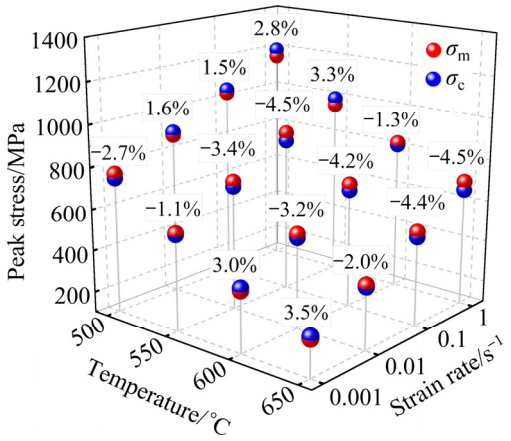

Fig. 8 Correlation between experimental and measured values of peak stress

3.3 Hot processing map

From the dynamic material model (DMM), the absorbed power (P) for hot working consists of J and G, where J is the energy consumed by microstructure evolution and G is the energy consumed by plastic deformation [26], which is written as

$$P=\sigma\cdot\dot{\varepsilon}=G+J=\int_0^{\dot{\varepsilon}}\sigma\mathrm{d}\dot{\varepsilon}+\int_0^{\sigma}\dot{\varepsilon}\mathrm{d}\sigma \tag{16}$$

The relationship between J and G can be described by the strain rate sensitivity (m) [8], which is expressed as follows:

$$m=\mathrm{d}J/\mathrm{d}G=[\dot{\varepsilon}\partial\sigma/\sigma\partial\dot{\varepsilon}]_{T\dot{\varepsilon}}=[\partial\ln\sigma/\partial\ln\dot{\varepsilon}]_{T\dot{\varepsilon}} \tag{17}$$

For a given ε, T, σ and $\dot{\varepsilon}$ satisfy a specific relationship as follows:

$$\sigma=K\dot{\varepsilon}^{m} \tag{18}$$

where K is material coefficient.

Dissipation energy can be written as

$$J=\int_0^{\sigma}\dot{\varepsilon}\mathrm{d}\sigma=(m\sigma\dot{\varepsilon})/(m+1) \tag{19}$$

"m=1" is regarded as ideal linear dissipation state, and J is up to the maximum value:

$$J=J_{\max}=\sigma\dot{\varepsilon}/2 \tag{20}$$

The coefficient efficiency of power dissipation (η) reflects the power dissipation characteristics for the nonlinear dissipation state, which can be

written as

$$\eta = J/J_{max} = 2m/(m+1) \quad (21)$$

From the extremum principle of irreversible thermodynamics [27], the instability criterion is expressed as

$$\xi(\dot{\bar{\varepsilon}}) = \partial \ln[m/(m+1)] / \partial \ln \dot{\bar{\varepsilon}} + m \quad (22)$$

where $\xi(\dot{\bar{\varepsilon}})$ is regarded as the function of T and $\dot{\varepsilon}$, and the negative value of $\xi(\dot{\bar{\varepsilon}})$ represents the instability region. At last, the processing map is acquired by combining the instability map and power dissipation map.

Figure 9(a) shows the 3D power dissipation map of the 60NiTi alloy at strains of 0.3, 0.35, 0.4 and 0.45. The different colors represent different values of η, and the darker the color is, the higher the power dissipation efficiency is, which is closer to ideal linear dissipation state. From Fig. 9(a), the region of the efficiency of power dissipation varied with true strain. When the true strain was 0.3, there were two peak power dissipation regions, namely 620−650 °C, 0.001−0.01 s^{-1} and 550−600 °C, 0.001−0.005 s^{-1}. The peak power dissipation regions varied with strain. When the true strain was 0.45, the peak power dissipation region was 600−650 °C, 0.005−0.05 s^{-1}. Figure 9(b) shows the 3D instability maps at different strains, where white region represents safe region and grey region represents instability region. Processing in instability region may result in shear bands, deformation twins and micro-cracks [28,29]. The instability region of the 60NiTi alloy gradually expanded with an increase in the true strain.

3.4 Microstructure evolution

3.4.1 Microstructure characterization of 60NiTi alloy

Figure 10 shows XRD pattern and SEM image of the as-extruded 60NiTi alloy. From Fig. 10(a), there were *B*2 phase matrix, Ni_3Ti phase and *B*19′ martensite in the alloy. The Ni content in matrix was reduced due to the precipitation of Ni_3Ti phase, which increased the phase temperature of the 60NiTi alloy and led to phase transformation from

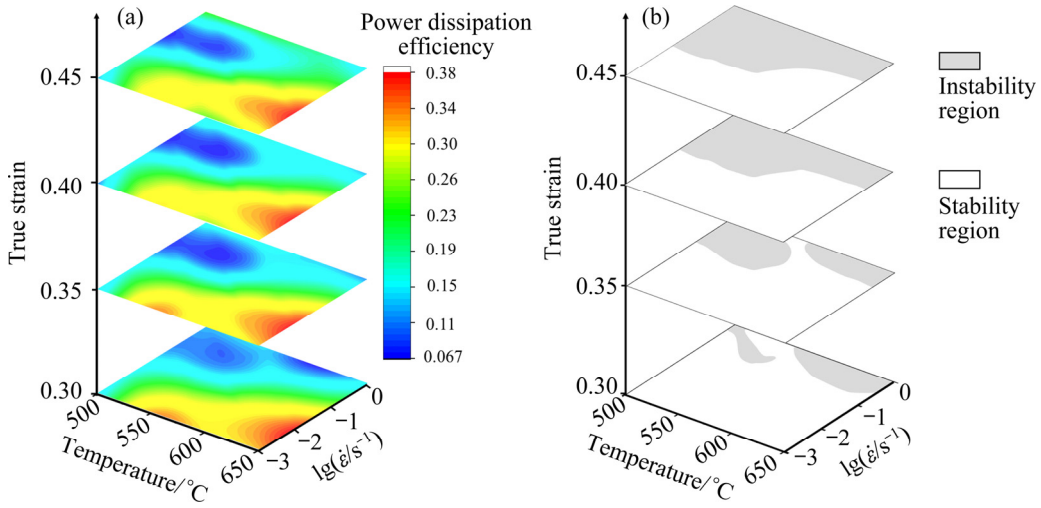

Fig. 9 3D power dissipation map (a) and 3D power instability map (b)

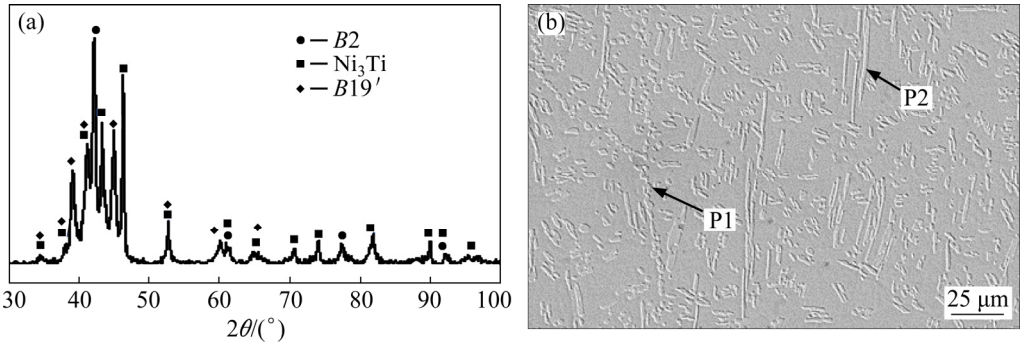

Fig. 10 XRD pattern (a) and SEM image (b) of as-extruded 60NiTi alloy

*B*2 to *B*19' [30]. From Fig. 10(b), after annealing, spherical precipitates (P1 in Fig. 10(b)), lenticular precipitates (P2 in Fig. 10(b)) were formed in the alloy, and the content of spherical precipitates was much higher than that of the lenticular precipitates. The chemical compositions of the phase were analyzed by EDS, as indicated in Table 1. The results of EDS and XRD showed that the spherical precipitates were Ni_3Ti phases and the lenticular precipitates were Ni_3Ti_2 phases. However, Ni_3Ti_2 phase was not detected by XRD due to its low content, $Ni_4Ti_3 \rightarrow Ni_3Ti_2 \rightarrow Ni_3Ti$ phase transition occurred during hot deformation [31], and Ni_3Ti_2 phase is a metastable phase, resulting in the low content of Ni_3Ti_2 phase.

Figure 11 shows the microstructure of the 60NiTi alloy under different compression conditions. After hot compression at 500 °C and 0.001 s^{-1}, a great number of dislocations piled up around grain boundaries, and some parallel deformation twins and a few DRX grains were observed, as shown in Fig. 11(a). By selected area electron diffraction (SAED), the red box was identified as $\{11\bar{1}\}$ type I twin with orientations of $[\bar{1}10]_M // [\bar{1}\,\bar{1}0]_{B2}$. $\{11\bar{1}\}$ type I twin belongs to transformation twins formed by the transformation of high symmetry *B*2 matrix to low symmetry *B*19′ martensite, which released the strain caused by phase transformation [32,33].

Table 1 Chemical composition of precipitates in 60NiTi alloy by EDS analysis

Precipitate	*x*(Ni)/at.%	*x*(Ti)/at.%
P1	73.9	26.1
P2	61.2	38.8

The *B*19′ martensite was observed in the sample after hot compression at 650 °C and 0.001 s^{-1}. Meanwhile, the spherical phase was identified as $(Ti_2Ni)_3O$ using EDS, i.e., 31.2 at.% Ti, 59.3 at.% Ni and 9.5 at.% O. The formation of *B*19′ martensite was discussed in Section 3.4.1. The $(Ti_2Ni)_3O$ phase with a diameter of 200 nm would be formed during the solidification at 984 °C [34]. During the hot compression, the $(Ti_2Ni)_3O$ phase particles impeded dislocation motion to form dislocation tangles, which provided large storing energy enough for inducing DRX in the matrix. Therefore, some DRX grains were formed around $(Ti_2Ni)_3O$ particles under the combined actions of temperature and strain, which can partially eliminate work hardening. Figure 11(c) shows the

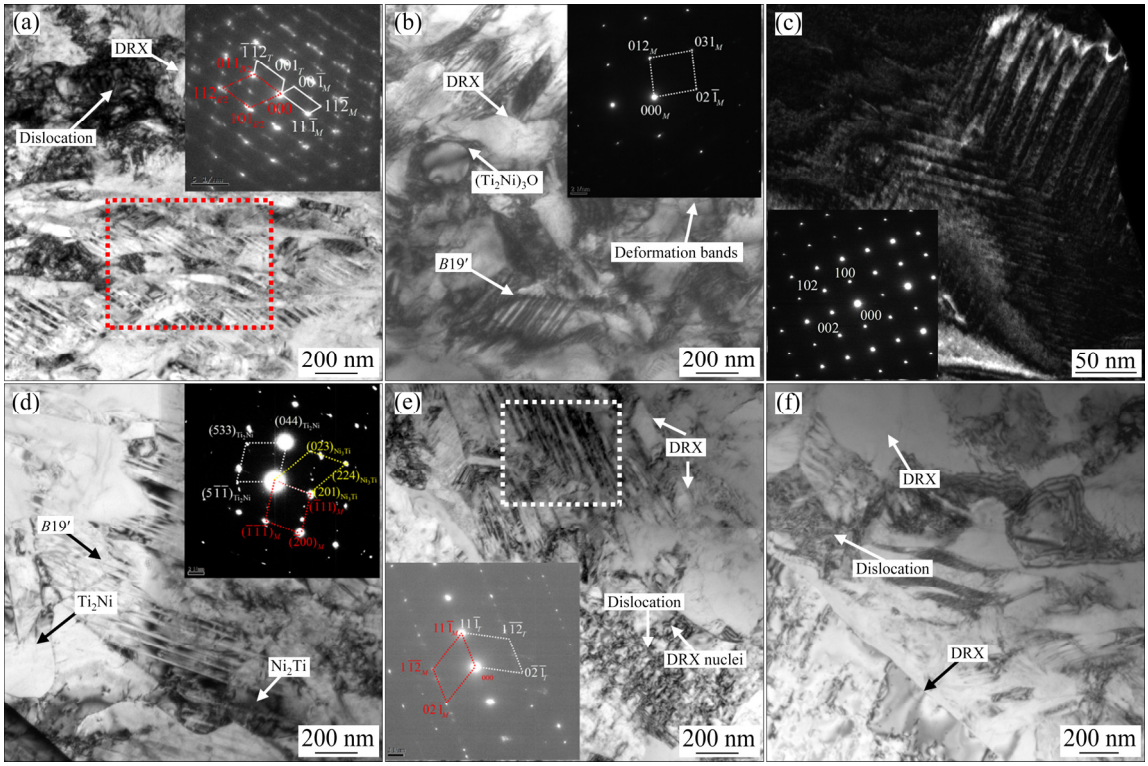

Fig. 11 Microstructures of 60NiTi alloy under different hot deformation conditions: (a) 500 °C, 0.001 s^{-1}; (b, c) 650 °C, 0.001 s^{-1}; (d) 650 °C, 0.01 s^{-1}; (e) 650 °C, 0.1 s^{-1}; (f) 650 °C, 1 s^{-1}

microstructure and selected area electron diffraction (SAED) pattern of strip-like Ni_3Ti phases, and the spacing between Ni_3Ti phases was about 25 nm.

After hot compression at 650 °C and 0.01 s^{-1}, the number of twins and the dislocation density rose obviously, and the ellipsoid Ti_2Ni and Ni_3Ti phases with numerous dislocation piling-up around were found. The orientation relationship between Ti_2Ni and Ni_3Ti, $B19'$ and Ti_2Ni, and $B19'$ and Ni_3Ti were $[0\bar{1}1]_M//[0\bar{1}1]_{Ti_2Ni}//[1\bar{3}2]_{Ni_3Ti}$, $(111)_M//(044)_{Ti_2Ni}$, and $(\bar{1}11)_M//(201)_{Ni_3Ti}$, as shown in Fig. 11(d). As the strain rate was 0.1 s^{-1}, there were numerous dislocations, sub-grain boundaries and DRX grains in the sample, as indicated in Fig. 11(e). During hot compression, sub-grain boundary transformed to large angle grain boundary by consuming abundant dislocations, which resulted in nucleation of DRX grains, as shown in Fig. 11(e). After the hot compression at 650 °C and 1 s^{-1}, DRX grains nucleated preferentially at the primary grain boundary and distributed in chains, which indicated the occurrence of discontinuous dynamic recrystallization (DDRX) [35].

According to the experimental results, the combination of dynamic recovery, dynamic recrystallization and twinning were the main hot deformation mechanisms of the 60NiTi alloy.

3.4.2 Relationship between microstructure and hot processing map

Figure 12 shows the hot processing map and microstructure of the 60NiTi alloy after hot compression at a true strain of 0.45. In the hot processing map of Fig. 12(a), the shadow region represents the instability region and the line indicates the value of η. In general, the higher η represents the better processability, and the lower η represents flow localization or unstable flow [17,36]. After the deformation under the conditions of high temperature and low strain rate, the value of η was relatively high, ~38%. As the deformation was carried out at medium temperature with low strain rate, the peak power efficiency region also occurred with η of ~32%, which was lower than that of high temperature with low strain rate. When the deformation was carried out at low temperature with high strain rate, the value of η was relatively low, ~8%. In addition, the region of high strain rate and low temperature was instability region, which was not suggested for hot working.

The value of η has great impact on deformation mechanism of the metallic material as follows [37−39]: (1) For η<0.3, DRV was the main softening mechanism; (2) For 0.3≤η<0.6, DRX was main softening mechanism; (3) For η>0.6, superplasticity was the main softening mechanism. The softening mechanism of the region was DRX as the sample was deformed at high temperature with medium−low strain rate (η>0.3), and the softening mechanism of region at low temperature with high strain rate (η<0.3) was dynamic recovery.

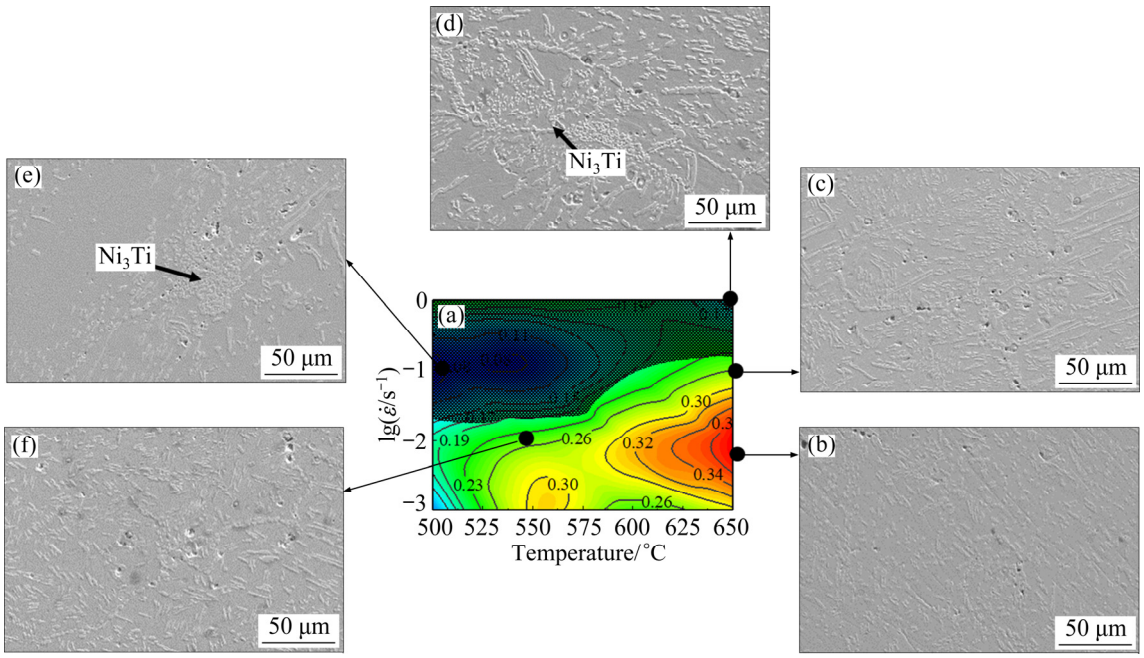

Fig. 12 Hot processing map (a) and SEM microstructures (b−f) of 60NiTi alloy after hot compression with true strain of 0.45: (b) 650 °C, 0.01 s^{-1}; (c) 650 °C, 0.1 s^{-1}; (d) 650 °C, 1 s^{-1}; (e) 500 °C, 0.1 s^{-1}; (f) 550 °C, 0.01 s^{-1}

Figures 12(b−f) show the microscopic structures of the 60NiTi alloy at various hot compression states. The phase particles were identified as Ni_3Ti by EDS analysis, i.e., 74.3 at.% Ni and 25.7 at.% Ti. From Fig. 12(d), the Ni_3Ti phase particles were uniformly distributed. While the strain rate grew, Ni_3Ti phase began to agglomerate and was continuously distributed at grain boundary with a strain rate of 1 s^{-1}, as indicated in Fig. 12(d). Figure 12(e) demonstrated the microstructure of the alloy at 500 °C and 0.1 s^{-1}, and many Ni_3Ti phase particles gathered, forming some local precipitate-free regions.

According to hot processing map and microstructure analysis of the 60NiTi alloy mentioned above, it can be determined that the smaller precipitates were uniformly distributed in high power dissipation region. With the decrease of power dissipation efficiency, the precipitates began to gather at grain boundary. In the region with the lowest power dissipation efficiency, a large number of Ni_3Ti phase particles gathered and many local precipitate-free zones were formed, which had adverse effect on the properties of the alloy [40,41]. Therefore, the hot processing parameters of the 60NiTi alloy can be determined as compression temperature of 600−650 °C and the strain rate of 0.005−0.05 s^{-1}.

4 Conclusions

(1) After annealing at 650 °C for 12 h, numerous spherical Ni_3Ti phase, and lenticular Ni_3Ti_2 phase were formed in the extruded 60NiTi alloy.

(2) Compression temperature as well as strain rate significantly affected the peak stress of the 60NiTi alloy. When strain rate remained constant, the peak stress decreased as the compression temperature increased. When the compression temperature remained constant, the peak stress increased as strain rate rose.

(3) The hot deformation activation energy Q of the 60NiTi alloy was 327.89 kJ/mol, and the peak stress constitutive equation was calculated as $\dot{\varepsilon} = 9.0\times10^{15}\times[\sinh(2.7\times10^{-3}\sigma)]^{5.7}\cdot\exp[-327887.5/(RT)]$. By plotting hot processing map, the proper hot processing parameters of the 60NiTi alloy were compression temperature of 600−650 °C and strain rate of 0.005−0.05 s^{-1}. The Ni_3Ti phase was uniformly distributed in the matrix at compression temperature of 650 °C with strain rate of 0.01 s^{-1}.

(4) When the compression temperature increased, the dynamic recrystallization degree increased. While the strain rate increased, the number of twin and dislocation density increased, and the Ni_3Ti phase tended to aggregate. Additionally, Ni_3Ti phase was beneficial to inducing dynamic recrystallization. The combined actions of the dynamic recovery, dynamic recrystallization and twinning were the main hot deformation mechanisms of the 60NiTi alloy.

Acknowledgments

This work was sponsored by the National Key Research and Development Program of China (No. 2020YFB0311102), the Ningbo “Science and Technology Innovation 2025” Major Project, China (No. 2019B10087), the Project of State Key Laboratory of Powder Metallurgy at Central South University and Young People Fund of Jiangxi Province, China (No. 2018BAB216005).

References

[1] CORTE C D, STANFORD M K, JETT T R. Rolling contact fatigue of superelastic intermetallic materials (SIM) for use as resilient corrosion resistant bearings [J]. Tribology Letters, 2015, 57(3): 1−10.

[2] INGOLE S. 60NiTi alloy for tribological and biomedical surface engineering applications [J]. JOM, 2013, 65(6): 792−798.

[3] CORTE C D. Novel super-elastic materials for advanced bearing applications [J]. Advances in Science and Technology, 2014, 89: 1−9.

[4] KHANLARI K, RAMEZANI M, KELLY P, CAO P, NEITZERT T. Mechanical and microstructural characteristics of as-sintered and solutionized porous 60NiTi [J]. Intermetallics, 2018, 100: 32−43.

[5] LEKSTON Z, ZUBKO M, PRUSIK K, STRÓŻ D. Microstructure, phase transformations, and properties of hot-extruded Ni-rich NiTi shape memory alloy [J]. Journal of Materials Engineering and Performance, 2014, 23(7): 2362−2367.

[6] HODGSON D, RUSSELL S. Nitinol melting, manufacture and fabrication [J]. Minimally Invasive Therapy & Allied Technologies, 2000, 9(2): 61−65.

[7] DEHGHANI K, KHAMEI A A. Hot deformation behavior of 60Nitinol (Ni60wt.%−Ti40wt.%) alloy: Experimental and computational studies [J]. Materials Science and Engineering A, 2010, 527: 684−690.

[8] WANG X, LI Z, XIAO Z, QIU W T. Microstructure evolution and hot deformation behavior of Cu−3Ti−0.1Zr alloy with ultra-high strength [J]. Transactions of Nonferrous

Metals Society of China, 2020, 30(10): 2737−2748.

[9] PANG Y, XIAO Z, JIA Y L, ZHANG R, YI J, QIU W T, LI Z. Hot deformation behavior of a CuAlMn shape memory alloy [J]. Journal of Alloys and Compounds, 2020, 845: 156161.

[10] LIU H N, LI Y J, ZHANG K, LI X G, MA M L, SHI G L, YUAN J W, WANG K K. Microstructure, hot deformation behavior, and textural evolution of Mg−3wt.%Zn−1wt.%Ca−0.5wt.%Sr alloy [J]. Journal of Materials Science, 2020, 55(32): 12434−12447.

[11] LI L H, QI F G, WANG Q, HOU C H, ZHAO N, YANG Y, CHAI S S, OUYANG X P. Hot deformation behavior of $Mg_{95.21}Zn_{1.44}Y_{2.86}Mn_{0.49}$ alloy containing LPSO phase [J]. Materials Characterization, 2020, 169: 110649.

[12] YEOM J T, KIM J H, HONG J K, KIM S W, PARK C H, NAM T H, LEE K Y. Hot forging design of as-cast NiTi shape memory alloy [J]. Materials Research Bulletin, 2014, 58: 234−238.

[13] JIANG S Y, ZHANG Y Q, ZHAO Y N, TANG M, YI W L. Constitutive behavior of Ni−Ti shape memory alloy under hot compression [J]. Journal of Central South University, 2013, 20(1): 24−29.

[14] MORAKABATI M, ABOUTALEBI M, KHEIRANDISH S, TAHERI A K, ABBASI S M. High temperature deformation and processing map of a NiTi intermetallic alloy [J]. Intermetallics, 2011, 19: 1399−1404.

[15] ZHANG Y Q, JIANG S Y, ZHAO Y N, LIU S W. Constitutive equation and processing map of equiatomic NiTi shape memory alloy under hot plastic deformation [J]. Transactions of Nonferrous Metals Society of China, 2016, 26(8): 2152−2161.

[16] CHAD H B, YU X X, NOEBE R D, MARTENS R, WEAVER M L, THOMPSON G B. Hardening behavior and phase decomposition in very Ni-rich Nitinol alloy s[J]. Materials Science and Engineering A, 2015, 639: 336−344.

[17] SARKAR A, KAPOOR R, VERMA A, CHAKRAVARTTY J K, SURI A K. Hot deformation behavior of Nb−1Zr−0.1C alloy in the temperature range 700−1700 °C [J]. Journal of Nuclear Materials, 2012, 422(1/2/3): 1−7.

[18] ZHANG Z H, JIANG Y B, CHEN Y T. Microstructure and deformation mechanism of Ag−12wt.%SnO_2 composite during hot compression [J]. Journal of Alloys and Compounds, 2017, 728: 719−726.

[19] LIU D K, LU Z, YU J X, SHI C C, XIAO H, LIU W, JIANG S S. Hot deformation behavior and microstructure evolution of NiAl−9HfO_2 composite [J]. Intermetallics, 2021, 139: 107344.

[20] HU Y L, LIN X, LI Y L, ZHANG S Y, GAO X H, LIU F G, LI X, HUANG W D. Plastic deformation behavior and dynamic recrystallization of Inconel 625 superalloy fabricated by directed energy deposition [J]. Materials & Design, 2020, 186: 108359.

[21] ROUZEGAR R, AZADBEH M, DANNINGER H. High-temperature flow behaviour modelling of stress–strain curves of the sintered Cu−28Zn pre-alloyed powder compacts considering dynamic recrystallization [J]. Powder Metallurgy, 2018, 61(1): 36−42.

[22] ZHANG H M, CHEN G, CHEN Q, HAN F, ZHAO Z D. A physically-based constitutive modelling of a high strength aluminum alloy at hot working conditions [J]. Journal of Alloys and Compounds, 2018, 743: 283−293.

[23] POLIAK E I, JONAS J J. A one-parameter approach to determining the critical conditions for the initiation of dynamic recrystallization [J]. Acta Materialia, 1996, 44: 127−136.

[24] ELETI R R, BHATTACHARJEE T, SHIBATA A, TSUJI N. Unique deformation behavior and microstructure evolution in high temperature processing of HfNbTaTiZr refractory high entropy alloy [J]. Acta Materialia, 2019, 171: 132−145.

[25] ZENER C, HOLLOMON J. Effect of strain rate upon plastic flow of steel [J]. Journal of Applied Physics, 1944, 15(1): 22−32.

[26] PRASAD Y, GEGEL H L, DORAIVELU S M, MALAS J C, MORGAN J T, LARK K A, BARKER D R. Modeling of dynamic material behavior in hot deformation: Forging of Ti-6242 [J]. Metallurgical Transactions A, 1984, 15(10): 1883−1892.

[27] PRASAD Y. Author's reply: Dynamic materials model: Basis and principles [J]. Metallurgical and Materials Transactions A, 1996, 27(1): 235−236.

[28] PRASAD Y. Processing maps: A status report [J]. Journal of Materials Engineering and Performance, 2003, 12(6): 638−645.

[29] RAMANATHAN S, KARTHIKEYAN R, GANASEN G. Development of processing maps for 2124Al/SiC_p composites [J]. Materials Science and Engineering A, 2006, 441: 321−325.

[30] FRENZEL J, GEORGE E P, DLOUHY A, SOMSEN C, WAGNER F X, EGGELER G. Influence of Ni on martensitic phase transformations in NiTi shape memory alloys [J]. Acta Materialia, 2010, 58: 3444−3458.

[31] ADHARAPURAPU R R, JIANG F, VECCHIO K S. Aging effects on hardness and dynamic compressive behavior of Ti−55Ni (at.%) alloy [J]. Materials Science and Engineering A, 2010, 527: 1665−1676.

[32] HU L, JIANG S Y, LIU S W, ZHANG Y Q, ZHAO Y N, ZHAO C Z. Transformation twinning and deformation twinning of NiTi shape memory alloy [J]. Materials Science and Engineering A, 2016, 660: 1−10.

[33] MA J, KARAMAN I, NOEBE R D. High temperature shape memory alloys [J]. International Materials Reviews, 2010, 55(5): 257−315.

[34] OTSUKA K, REN X. Physical metallurgy of Ti–Ni-based shape memory alloys [J]. Progress in Materials Science, 2005, 50(5): 511−678.

[35] LI B, DU Y, CHU Z J, ZHOU W, YANG X L. Research on dynamic recrystallization behavior of NiFeCr based alloy [J]. Materials Characterization, 2020, 169: 110653.

[36] CHAUDHURI A, BEHERA A N, SARKAR A, KAPOOR R, RAY R K, SUWAS S. Hot deformation behaviour of Mo-TZM and understanding the restoration processes involved [J]. Acta Materialia, 2019, 164: 153−164.

[37] LI C M, HUANG L, ZHAO M J, ZHANG X T, LI J J, LI P C. Influence of hot deformation on dynamic recrystallization behavior of 300M steel: Rules and modeling [J]. Materials Science and Engineering A, 2020, 797: 139925.

[38] WANG K L, LU S Q, FU M W, LI X, DONG X J. Optimization of β/near-β forging process parameters of

Ti−6.5Al−3.5Mo− 1.5Zr−0.3Si by using processing maps [J]. Materials Characterization, 2009, 60: 492−498.

[39] ZHANG X X, YAN Q Z, YANG C T, WANG T N, GE C C. Microstructure, mechanical properties and bonding characteristic of deformed tungsten [J]. International Journal of Refractory Metals and Hard Materials, 2014, 43: 302−308.

[40] SANDERS T H, STARKE E A. The effect of slip distribution on the monotonic and cyclic ductility of AlLi binary alloys [J]. Acta Metallurgica, 1982, 30: 927−939.

[41] PARDOEN T, DUMONT D, DESCHAMPS A, BRECHET Y. Grain boundary versus transgranular ductile failure [J]. Journal of the Mechanics and Physics of Solids, 2003, 51(4): 637−665.

60NiTi 合金的热压缩变形与显微组织演变

陈 东[1]，杨倩如[1]，杨纳川[1]，王 檬[1]，徐 强[1]，
吴静远[1]，姜雁斌[1,2]，李 周[1,3]，肖 柱[1,3]，魏海根[4]

1. 中南大学 材料科学与工程学院，长沙 410083；
2. 中南大学 有色金属材料科学与工程教育部重点实验室，长沙 410083；
3. 中南大学 粉末冶金国家重点实验室，长沙 410083；
4. 江西理工大学 材料冶金化学学部，赣州 341000

摘 要：采用 Gleeble−3500 热模拟试验机对在变形温度 500~650 ℃和应变速率 0.001~1 s^{-1} 条件下的 60NiTi 合金进行热压缩变形，分析其热变形行为和显微组织，建立变形本构模型，绘制热加工图。结果表明，当压缩温度升高或应变速率降低时，峰值应力减小。合金的热变形激活能为 327.89 kJ/mol，热加工工艺参数为变形温度 600~650 ℃和应变速率 0.005~0.05 s^{-1}。当变形温度升高时，合金的再结晶程度增大；当应变速率增大时，位错密度和孪晶数量增大，Ni_3Ti 相易于聚集；Ni_3Ti 析出相有利于诱发合金基体的动态再结晶。动态回复、动态再结晶和孪生是 60NiTi 合金热变形的主要机制。

关键词：60NiTi 合金；热压缩变形；显微组织；动态再结晶

(Edited by Bing YANG)